Bergische Universität Wuppertal

Fakultät für Mathematik und Naturwissenschaften

Institute of Mathematical Modelling, Analysis and Computational Mathematics (IMACM)

Preprint BUW-IMACM 25/01

Reza Taherdangkoo, Mostafa Mollaali, Matthias Ehrhardt, Thomas Nagel, Lyesse Laloui, Alessio Ferrari, and Christoph Butscher

A finite element-based machine learning model for hydro-mechanical analysis of swelling behavior in clay-sulfate rocks

January 20, 2025

http://www.imacm.uni-wuppertal.de

A finite element-based machine learning model for hydro-mechanical analysis of swelling behavior in clay-sulfate rocks

Reza Taherdangkoo[1], *Mostafa Mollaali*[2], *Matthias Ehrhardt*[3], *Thomas Nagel*[1], *Lyesse Laloui*[4], *Alessio Ferrari*[4], *and Christoph Butscher*[1]

[1]*TU Bergakademie Freiberg, Geotechnical Institute, Gustav-Zeuner-Str. 1, 09599 Freiberg, Germany*

[2]*Helmholtz Centre for Environmental Research– UFZ, Department of Environmental Informatics, Leipzig, 04318, Germany*

[3]*Applied and Computational Mathematics, Bergische Universität Wuppertal, Wuppertal, Germany*

[4]*École Polytechnique Fédérale de Lausanne (EPFL), Laboratory of Soil Mechanics, Lausanne, Switzerland*

Corresponding author, Reza.Taherdangkoo@ifgt.tu-freiberg.de

Abstract

The hydro-mechanical behavior of clay-sulfate rocks, especially their swelling properties, poses significant challenges in geotechnical engineering. This study presents a hybrid constrained machine learning (ML) model developed using the categorical boosting algorithm (CatBoost) tuned with a Bayesian optimization algorithm to predict and analyze the swelling behavior of these complex geological materials. Initially, a coupled hydro-mechanical model based on the Richards' equation coupled to a deformation process with linear kinematics implemented within the finite element framework OpenGeoSys was used to simulate the observed ground heave in Staufen, Germany, caused by water inflow into the clay-sulfate bearing Triassic Grabfeld Formation. A systematic parametric analysis using Gaussian distributions of key parameters, including Young's modulus, Poisson's ratio, maximum swelling pressure, permeability, and air entry pressure, was performed to construct a synthetic database. The ML model takes time, spatial coordinates, and these parameter values as inputs, while water saturation, porosity, and vertical displacement are outputs. In addition, penalty terms were incorporated into the CatBoost objective function to enforce physically meaningful predictions. Results show that the hybrid approach effectively captures the nonlinear and dynamic interactions that govern hydro-mechanical processes. The study demonstrates the ability of the model to predict the swelling behavior of clay-sulfate rocks, providing a robust tool for risk assessment and management in affected regions. The results highlight the potential of ML-driven models to address complex geotechnical challenges.

Keywords: clay-sulfate rocks; swelling; hydro-mechanical modeling; physics-based machine learning; categorical boosting

1 Introduction

The swelling behavior of clay-sulfate rocks is a major challenge in geotechnical engineering. This phenomenon is most commonly observed in geological formations that contain both clay minerals and anhydrite, such as the Triassic Grabfeld Formation (formerly known as the "Gypsum Keuper") in southern Germany and Switzerland (Butscher et al., 2016; Taherdangkoo et al., 2023). The swelling is triggered by water infiltration, leading to two distinct but interrelated mechanisms: the interlayer hydration and osmotic swelling of clay minerals, and the transformation of anhydrite ($CaSO_4$) into gypsum ($CaSO_4 \cdot 2\,H_2O$) in a hydration reaction. The latter mechanism, known as gypsification, is particularly important because it is associated with an increase in volume of up to 61 %. This expansion induces significant swelling pressures that often exceed the bearing capacity of surrounding soils or structures, leading to ground heave, structural damage, and failure of the affected infrastructure (Butscher et al., 2016; Madsen & Müller-Vonmoos, 1989).

The complexity of swelling in clay-sulfate rocks results from the coupled interactions between hydraulic, mechanical, and chemical processes. For example, the chemical transformation of anhydrite to gypsum changes the pore structure, affecting permeability and porosity. This change, in turn, affects the hydraulic response of the rock, influencing the dynamics of water flow. At the same time, the induced swelling pressures cause mechanical deformations that alter the hydraulic behavior (Schweizer et al., 2018; Wanninger, 2020). These coupled processes are nonlinear and time-dependent, often spanning years or decades (Taherdangkoo et al., 2023; Wittke, 2014). In addition, self-sealing behavior caused by gypsum coating on anhydrite inhibits mineral dissolution, introducing a feedback mechanism that makes swelling behavior difficult to predict. Environmental factors such as changes in groundwater flow, stress conditions, and pore water chemistry further exacerbate the uncertainty in predicting swelling response (Butscher et al., 2011; Jarzyna et al., 2022).

Despite decades of research, understanding and managing the swelling behavior of clay-sulfate rocks remains a complex task (Alonso, 2023; Taherdangkoo et al., 2024a; Wanninger, 2020). Numerical modeling, particularly finite element modeling (FEM), has been widely used to study the swelling of expansive geomaterials. FEM provides an established approach to solving the physics-based coupled hydro-mechanical-chemical equations that govern swelling, allowing the simulation of complex interactions with high fidelity. However, the computational cost of FEM simulations increases significantly when applied to large-scale systems or when the variability and uncertainty of input parameters must be considered (Buchwald et al., 2020). The need for repeated evaluations when performing sensitivity analyses, uncertainty quantification, and parameter optimization, often limits FEM-based simulations for many real-world applications (Buchwald et al., 2024).

The emergence of machine learning (ML) offers a promising alternative to address these limitations. ML models are particularly well suited for problems characterized by nonlinear relationships and high-dimensional parameter spaces, such as the swelling behavior of clay-sulfate rocks (Burden & Winkler, 2009; Taherdangkoo et al., 2022b). ML models can learn the underlying patterns and dependencies between input parameters and outputs by training on data sets generated from FEM simulations or field measurements (Virupaksha et al., 2024). Once trained, these models can provide predictions orders of magnitude faster than FEM, making them invaluable for real-time analysis, optimization, or risk assessment. However, a key challenge in applying ML to geotechnical problems is ensuring that the predictions remain physically consistent, as purely data-driven ML models run the risk of producing outputs that are physically implausible (Kooti et al., 2024; Taherdangkoo et al., 2024b).

This study addresses these challenges by developing a hybrid modeling framework that combines physics-based FEM with constrained ML to predict and analyze the swelling behavior of clay-sulfate rocks. The FEM model focuses on hydro-mechanical processes and incorporates swelling pressures as a function of water saturation to indirectly account for chemical contributions to volumetric strain, allowing efficient prediction of deformation and porosity changes. First, a coupled hydro-mechanical model – based on Richards' equation and linear kinematics – implemented within the OpenGeoSys framework was used to simulate the observed ground heave at Staufen, Germany. A systematic parametric analysis was performed to construct a synthetic database that was used to train a constrained machine learning model. This model, developed using the categorical boosting algorithm (CatBoost) and optimized with Bayesian methods, integrates time, spatial coordinates, and material properties as inputs to predict the

evolution of porosity, saturation, and vertical displacement during swelling. We then quantified parametric uncertainties using Monte Carlo simulations.

2 Problem statement

The rock swelling occurred following the failure of geothermal drilling operations in 2007 in the town of Staufen in southwestern Germany. The wellbore failure resulted in upward flow of water from underlying artesian aquifers into the Grabfeld formation, a clay layer characterized by significant anhydrite content. The interaction of the water with sulfate minerals caused both mechanical swelling of the clay and chemical swelling through anhydrite gypsification. These processes led to a significant increase in volume of the rock mass, resulting in long-term ground deformations (Grimm et al., 2014; Ruch & Wirsing, 2013; Schweizer et al., 2019).

In response, a number of mitigation measures were implemented in 2009 (LGRB, 2010). These measures included the re-grouting of the defective boreholes and the installation of pumping wells in the artesian aquifer beneath the Grabfeld formation. Their goal was to lower the hydraulic potential in the aquifer, thereby reducing water intrusion into the clay-sulfate rocks and mitigating further swelling. The Geological Survey of Baden-Württemberg (LGRB) established a geodetic network with 106 observation points. The ground surface displacement was recorded from January 2008 to September 2011, with each point being sampled up to 49 times at intervals of 11 to 63 days (LGRB, 2010, 2012).

3 Finite element method

A machine learning model was developed based on a previously established hydro-mechanical (HM) finite element framework to simulate the swelling behavior of clay-sulfate rocks in the geological setting of Staufen, Germany (Taherdangkoo et al., 2022a).

3.1 Mathematical model and numerical implementation

A summary of the governing equations is presented here, with more comprehensive details available in Taherdangkoo et al. (2022a). The fluid flow within the porous media is governed by the Richards' equation (Kafle et al., 2022; Pitz et al., 2023):

$$\rho_{\mathrm{w}}\left[\phi+\frac{p_{\mathrm{w}}S_{\mathrm{w}}(\alpha_{\mathrm{B}}-\phi)}{K_{\mathrm{s}}}\right]\dot{S}_{\mathrm{w}}+\rho_{\mathrm{w}}S_{\mathrm{w}}\left[\frac{\phi}{K_{\mathrm{w}}}+S_{\mathrm{w}}\frac{\alpha_{\mathrm{B}}-\phi}{K_{\mathrm{s}}}\right]\dot{p}_{\mathrm{w}}+\nabla\cdot\mathbf{q}+\alpha_{\mathrm{B}}\rho_{\mathrm{w}}S_{\mathrm{w}}\nabla\cdot\dot{\mathbf{u}}=0, \quad (1)$$

where ϕ is the porosity, ρ_{w} is the water density, and S_{w} is the water saturation, p_{w} is the water pressure, $\mathbf{u}$ the displacement of the solid skeleton, and $\mathbf{q}$ is the Darcy mass flux.

The Biot-Willis coefficient is α_{B}, and the bulk moduli of the solid and water phase are K_{s} and K_{w}, respectively. The relation between capillary pressure and saturation was described by Van Genuchten (1980).

The mechanical equilibrium is described by:

$$\nabla\cdot\boldsymbol{\sigma}+\left[\rho_{\mathrm{s}}(1-\phi)+S_{\mathrm{w}}\rho_{\mathrm{w}}\phi\right]\mathbf{g}=\mathbf{0}, \quad (2)$$

where ρ_{s} is the intrinsic solid density and $\boldsymbol{\sigma}$ is the total stress tensor. The relationship between the total stress tensor, $\boldsymbol{\sigma}$, and the effective stress tensor, $\boldsymbol{\sigma}'$, follows the extended Bishop's model:

$$\boldsymbol{\sigma}=-\chi(S_{\mathrm{w}})p_{\mathrm{w}}\mathbf{I}+\boldsymbol{\sigma}'-\sigma^{\mathrm{sw}}\mathbf{I}, \quad (3)$$

where $\chi(S_{\mathrm{w}})$ is Bishop's function, often set equal to the water saturation S_{w}. The unit tensor is denoted by $\mathbf{I}$, and σ^{sw} represents the swelling pressure. The swelling behavior is described by relating the swelling pressure σ^{sw} to the maximum swelling pressure, $\sigma^{\mathrm{sw}}_{\mathrm{max}}$, and to the change in water saturation via (Chaudhry et al., 2024; Taherdangkoo et al., 2022a):

$$\sigma^{\mathrm{sw}}=\sigma^{\mathrm{sw}}_{\mathrm{max}}(S_{\mathrm{w}}-S_{\mathrm{wi}}) \quad (4)$$

The described processes were implemented using OpenGeoSys (OGS) (Bilke et al., 2019; Kolditz et al., 2012), a finite element-based simulator for solving coupled processes in porous media.

3.2 Numerical model setup

The axisymmetric 2D domain extends horizontally for $240\,\mathrm{m}$ and vertically for $104.5\,\mathrm{m}$, and includes two layers: the swelling layer ($42.5\,\mathrm{m}$) and the overburden layer ($62\,\mathrm{m}$) Figure 1. The overburden layer represents the consolidation of all layers above the swelling layer into a single equivalent layer. The sedimentary layers are treated as homogeneous throughout the domain.

The simulation proceeds in three phases: (1) establishment of a steady-state initial condition, (2) water inflow into the swelling layer following geothermal drilling on 3 September 2007, and (3) stopping of the water inflow as a result of mitigation measures initiated on 4 November 2009. The total simulation time for phases (2) and (3) was 1490 days, with 790 days for the leakage period and 710 days for the mitigation phase (LGRB, 2010, 2012).

During the leakage phase, water entered the swelling layer ($-104.5\,\mathrm{m} \leq y \leq -62\,\mathrm{m}$) through the left boundary at a constant inflow rate of $1.3{\cdot}10^{-1}\,\mathrm{kg\,s^{-1}}$ (Schweizer et al., 2018). The inflow was distributed over the boundary using a normalized Neumann flux boundary condition, with the normalization based on the borehole radius to represent the effective cross-sectional area for water entry into the domain. In the mitigation phase (710 days), the inflow was stopped and this boundary was switched to a no-flow condition. The right boundary ($-104.5\,\mathrm{m} \leq y \leq 0\,\mathrm{m}$) was kept at the initial pressure, while the top boundary was defined as a free drainage surface and kept constant at its initial pressure. The model assumes pure water with a density of $1000\,\mathrm{kg\,m^{-3}}$ for both ambient and inflowing water, despite known variations in groundwater composition (LGRB, 2010). Mechanically, the lateral and bottom boundaries were fixed in the normal direction, while the top boundary was traction-free.

The elastic and hydrogeological parameters were obtained from (Benz & Wehnert, 2012; LGRB, 2010, 2012; Schweizer et al., 2018). The properties of the overburden layer were calculated as a weighted arithmetic mean of the geological layers. The material parameters used in the simulations are listed in Table 1.

Table 1: Material parameter values used in the finite element model.

Property	Units	Swelling layer	Overburden layer
Young's modulus (E)	MPa	500	1000
Poisson's ratio (ν)	-	0.2	0.2
Biot-Willis coefficient (α_B)	-	1	1
Maximum swelling pressure ($\sigma^{\mathrm{sw}}_{\mathrm{max}}$)	MPa	8	0
Porosity (ϕ)	-	0.077	0.14
Intrinsic permeability (k)	$\mathrm{m^2}$	$2 \cdot 10^{-13}$	$8 \cdot 10^{-13}$
Solid density (ρ_s)	$\mathrm{kg\,m^{-3}}$	2670	2627
Water Density (ρ_w)	$\mathrm{kg\,m^{-3}}$	1000	1000
Water viscosity (μ_w)	$\mathrm{Pa \cdot s}$	10^{-3}	10^{-3}
Initial water saturation (S_wi)	-	0.13	0.13
Van Genuchten parameter (m)	-	0.75	0.75
Van Genuchten air entry pressure ($\mathrm{p_b}$)	Pa	2000	2000

3.3 Sensitivity analysis

A one-variable-at-a-time (OVAT) sensitivity analysis was performed to generate a synthetic data set for machine learning modeling. The analysis involved systematically varying key parameters of the clay-sulfate layer, including Young's modulus (E), Poisson's ratio (ν), maximum swelling pressure ($\sigma^{\mathrm{max}}_{sw}$), permeability ($k$), and air entry pressure (p_b). Throughout the analysis, the material properties of the overburden were held constant. The base values and corresponding ranges for these parameters are shown in Table 2.

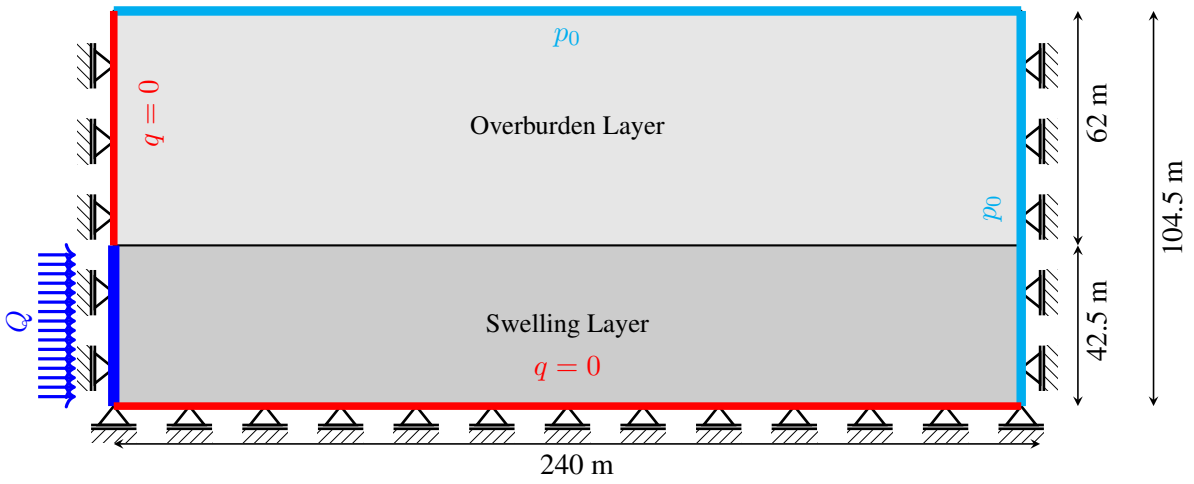

(a)

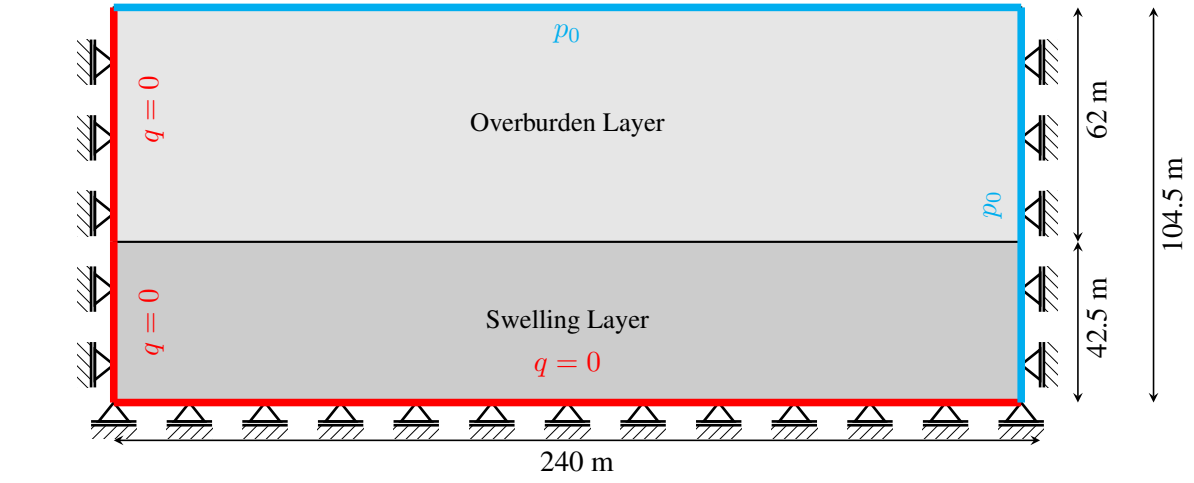

(b)

Figure 1: A schematic view of the numerical model illustrating the flow and mechanical boundary conditions during (a) the leakage period and (b) the mitigation period.

Table 2: Parameter values used for the sensitivity analysis of the swelling layer.

Parameters	Units	Base Value	Minimum	Maximum
Young's modulus (E)	MPa	500	300	2500
Poisson's ratio (ν)	-	0.2	0.16	0.35
Swelling pressure ($\sigma_{\text{max}}^{\text{sw}}$)	MPa	8	3.2	13
Permeability (k)	m^2	$2 \cdot 10^{-13}$	10^{-14}	10^{-12}
Air entry pressure (p_{b})	Pa	2000	1000	3500

To systematically explore the parameter space, 30 values were generated for each parameter using Gaussian distributions centered on their base values. The standard deviations for these distributions were determined as follows:

$$s_{\text{param}} = \frac{\text{max}_{\text{param}} - \text{min}_{\text{param}}}{3}, \tag{5}$$

where $\text{max}_{\text{param}}$ and $\text{min}_{\text{param}}$ represent the maximum and minimum values of each parameter's range, respectively. This approach resulted in a total of 150 parameter sets, which were then used to perform simulation runs.

4 Machine learning model

4.1 CatBoost algorithm

The machine learning algorithm used, CatBoost, is a gradient boosting method designed for efficient handling of categorical features and improved generalization. It iteratively constructs an ensemble of decision trees, where each tree is trained to minimize the residual errors of the preceding trees. For regression tasks, the general objective function in gradient boosting can be written as (Dorogush et al., 2018; Prokhorenkova et al., 2018):

$$\mathcal{L}(\mathbf{y}, \hat{\mathbf{y}}) = \sum_{i=1}^{n} \ell(y_i, \hat{y}_i) + \Omega(\Theta), \tag{6}$$

where y_i is the true value for the i^{th} sample obtained from the finite element analysis, $\hat{y}_i$ is the predicted value, and $\ell(y_i, \hat{y}_i)$ denotes the loss function. The regularization term $\Omega(\Theta)$ depends on the model parameters Θ and is used to prevent overfitting. At each iteration t, the model fits a decision tree $h_t(x)$ to the negative gradient of the loss function:

$$h_t(x) \approx g_t = -\nabla_{\hat{y}_{t-1}} \mathcal{L}(y, \hat{y}_{t-1}), \tag{7}$$

where $\mathbf{g}_t$ is the decent direction for the boosting step t. The predictions are then updated as:

$$\hat{y}_t = \hat{y}_{t-1} + \eta \cdot h_t(x), \tag{8}$$

where η is the learning rate, controlling the contribution of each tree. To enforce physically meaningful predictions, the standard loss function (e.g., mean squared error, MSE) is modified with custom penalties. The penalized loss function is defined as

$$\mathcal{L}_{\text{total}} = \frac{1}{n} \sum_{i=1}^{n} \left[(y_i - \hat{y}_i)^2 + \alpha \cdot \text{Penalty}(y_i, \hat{y}_i) \right], \tag{9}$$

where α is the penalty scale. Linear, exponential, or quadratic penalties were applied separately to each output variable – porosity, saturation, and displacement – with the threshold $\tau > 0$ adjusted based on the magnitude of the residuals for each variable. The penalty functions are defined as follows

$$\text{Penalty}_{\text{linear}} = \frac{1}{n} \sum_{i=1}^{n} \max\left(0, \alpha(|y_i - \hat{y}_i| - \tau)\right), \tag{10}$$

$$\text{Penalty}_{\text{quadratic}} = \frac{1}{n} \sum_{i=1}^{n} \max\left(0, \alpha(|y_i - \hat{y}_i| - \tau)^2\right), \tag{11}$$

$$\text{Penalty}_{\text{exponential}} = \frac{1}{n} \sum_{i=1}^{n} \max\left(0, e^{\alpha(|y_i - \hat{y}_i| - \tau)} - 1\right), \tag{12}$$

Bayesian optimization was used to tune the hyperparameters, including the number of trees (n_estimators), the maximum tree depth (max_depth), the learning rate (η), the L2 regularization term (λ), and the penalty scale (α). Optimal configurations were determined separately for each output variable to effectively train the CatBoost models.

4.2 Bayesian optimization

Bayesian optimization was used to systematically tune the hyperparameters and minimize the penalized loss function $\mathcal{L}_{\text{total}}$. The surrogate model, $\mathcal{P}(\mathcal{O}(\theta))$, was modeled as a Gaussian process (GP) (Foresee & Hagan, 1997; Snoek et al., 2012; Taherdangkoo et al., 2021):

$$\mathcal{P}(\mathcal{O}(\theta)) \sim \mathcal{GP}(\mu(\theta), k(\theta, \theta')), \tag{13}$$

where $\mu(\theta)$ is the mean function and $k(\theta, \theta')$ is the kernel function that captures the similarity between two hyperparameter configurations θ and θ'. To select the next set of hyperparameters to evaluate, the expected improvement (EI) detection function was used, written as

$$\mathrm{EI}(\theta) = \mathbb{E}\left[\max(0, \mathcal{O}(\theta) - \mathcal{O}_{\text{best}})\right], \tag{14}$$

where $\mathcal{O}_{\text{best}}$ is the best objective value observed so far. The EI balances the trade-off between exploring regions of high uncertainty and exploiting regions that are likely to yield improvements near the current optimum.

The optimization process was initialized with 10 randomly sampled configurations to construct an initial GP surrogate model. The model was then iteratively refined over 140 optimization steps to converge on the best set of hyperparameters. During optimization, penalty contributions were tracked, allowing analysis of the impact of each output variable on the penalized loss function. The objective function minimized in this process was the negative penalized loss

$$\mathcal{O}(\theta) = -\mathcal{L}_{\text{total}}(\mathbf{y}, \hat{\mathbf{y}}). \tag{15}$$

5 Monte Carlo simulation

Monte Carlo simulation was used to quantify the uncertainty in the model predictions (Metropolis & Ulam, 1949) using the trained ML model. A total of $N = 30\,000$ samples were generated for $M = 5$ parameters: Young's modulus (E), Poisson's ratio (ν), permeability (K), air entry pressure (p_b), and maximum swelling pressure ($\sigma_{\text{max}}^{\text{sw}}$). The scaled value for the i^{th} sample and the j^{th} parameter was calculated as follows:

$$x_{\text{scaled},i,j} = x_{\min,j} + (x_{\max,j} - x_{\min,j}) \cdot x_{\text{random},i,j}, \tag{16}$$

where $x_{\text{random},i,j}$ is a random number uniformly sampled from $[0, 1]$, and $x_{\min,j}$ and $x_{\max,j}$ are the minimum and maximum values for the j^{th} parameter, respectively. This scaling ensures a consistent distribution of the parameters across their respective ranges. In addition to these primary parameters, three auxiliary features (i.e. time and coordinate systems) were sampled directly from the dataset. Random sampling with replacement (Taherdangkoo et al., 2024b) was performed to draw N samples of the features time_value, x_s, and y_s from the dataset according to

$$\text{time\_value}_i, \quad x_{s,i}, \quad y_{s,i}, \quad i = 1, 2, \ldots, N. \tag{17}$$

The final input matrix, $\mathbf{X}_{\text{final}}$, was constructed by combining the scaled Monte Carlo data with the randomly sampled auxiliary features:

$$\mathbf{X}_{\text{final}} = \begin{bmatrix} \text{time\_value}_1 & E_1 & \nu_1 & k_1 & p_{b,1} & \sigma_{\text{max}\,1}^{\text{sw}} & x_{s,1} & y_{s,1} \\ \text{time\_value}_2 & E_2 & \nu_2 & k_2 & p_{b,2} & \sigma_{\text{max}\,2}^{\text{sw}} & x_{s,2} & y_{s,2} \\ \vdots & \vdots & \vdots & \vdots & \vdots & \vdots & \vdots & \vdots \\ \text{time\_value}_N & E_N & \nu_N & k_N & p_{b,N} & \sigma_{\text{max}\,N}^{\text{sw}} & x_{s,N} & y_{s,N} \end{bmatrix}.$$

Each row of $\mathbf{X}_{\text{final}}$ represents a complete feature vector for one Monte Carlo sample. This dataset was then used to analyze the variability of the model outputs, enabling quantification of the uncertainty associated with the predictions.

6 Results and discussion

6.1 Model performance assessment

The data set obtained from the sensitivity analysis contains approximately $5.4745 \cdot 10^7$ entries. It includes the parameters listed in Table 2 along with porosity, saturation, and displacement values at 19209 finite element node and 25 time step for 114 simulations. The distributions of the aforementioned parameter values across the entire dataset are depicted in Figure 2.

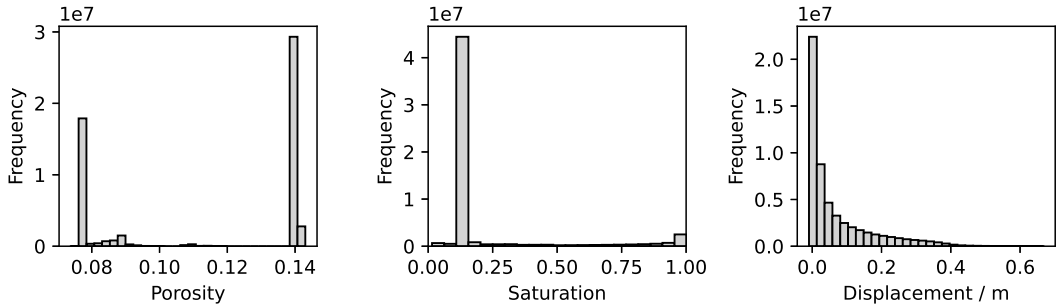

Figure 2: Histograms showing the distribution of porosity, saturation, and displacement values for the entire dataset.

Given the large size of the dataset, a $4:1$ splitting method was used to divide the data into training and test subsets. This approach ensures computational efficiency while maintaining a sufficiently large and representative test set for model evaluation. The random seed was set to 42 for reproducibility, allowing consistent validation of results across runs.

We ran several simulations to determine the optimal hyperparameter bounds of the CatBoost model, the number of iterations for the optimization process, the type of penalty function, and the size of the threshold τ for each output variable. The loss function was eventually modified with a linear penalty for porosity, an exponential penalty for saturation, and a quadratic penalty for displacement. A residual threshold of 0.001 was applied uniformly to all three variables.

Figures 3–5 illustrate the Bayesian optimization of the porosity, saturation, and displacement models over 150 iterations, and Table 3 lists the optimal hyperparameter configurations. Figure 3 shows high variability in early iterations, indicating exploration of the hyperparameter space. The porosity model stabilizes around iteration 120, indicating convergence to an optimal solution. Iteration 124 achieves the lowest penalized MSE ($1.272 \cdot 10^{-6}$), balancing model accuracy (MSE of $1.208 \cdot 10^{-8}$) and regularization (penalty term of $1.259 \cdot 10^{-6}$). The convergence pattern highlights the effectiveness of the optimization strategy in improving generalization.

The saturation model (Figure 4) optimizes at iteration 77, with an MSE of $5.177 \cdot 10^{-5}$, a penalty term of $1.545 \cdot 10^{-3}$, and a penalized MSE of $1.597 \cdot 10^{-3}$. This iteration demonstrates an optimal trade-off between prediction accuracy and regularization, as reflected in the minimized penalized MSE. The displacement model (Figure 5) optimizes at iteration 104, yielding an MSE of $9.458 \cdot 10^{-7}$, a penalty term of $1.664 \cdot 10^{-4}$, and a penalized MSE of $1.673 \cdot 10^{-4}$. This iteration effectively balances accuracy and regularization, with minimal trade-off in predictive performance due to regularization.

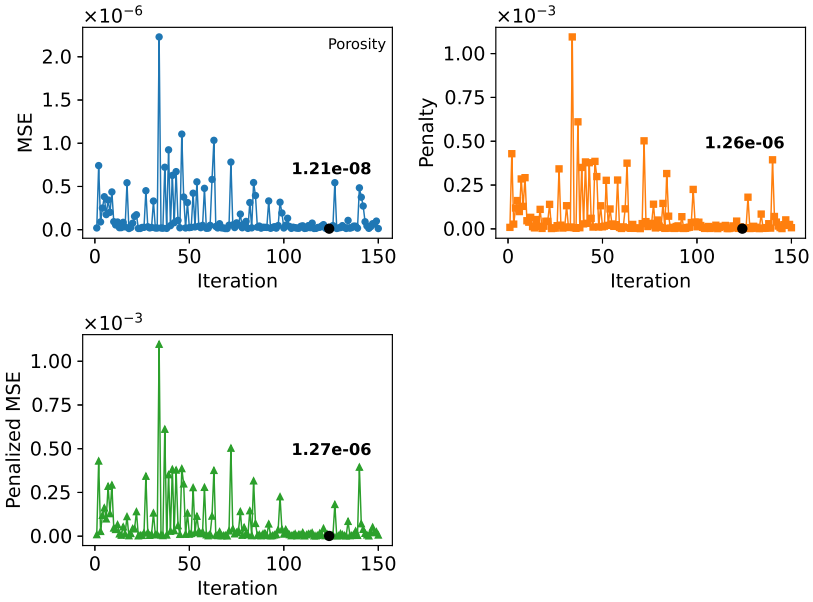

Figure 3: The evolution of MSE, penalty term, and penalized MSE during hyperparameter tuning of the porosity model. Iteration 124 corresponds to the optimized parameter set.

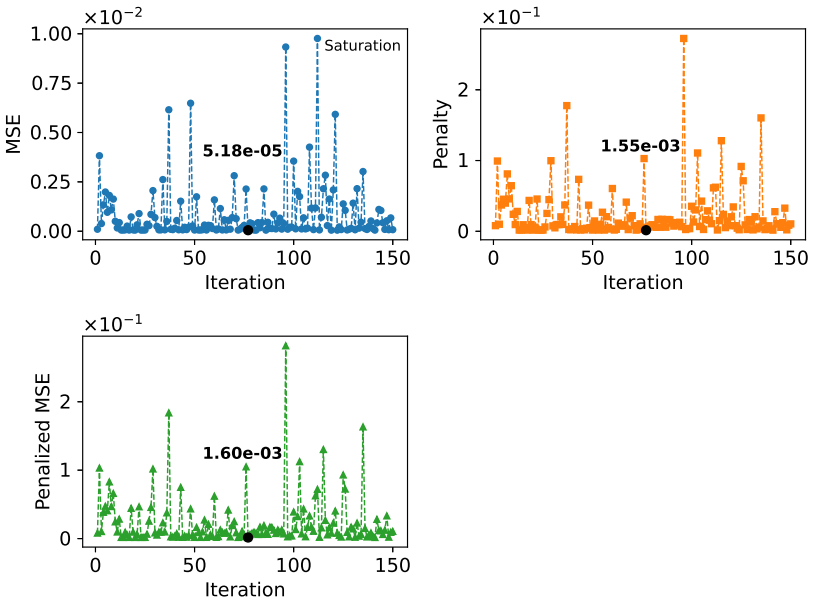

Figure 4: The evolution of MSE, penalty term, and penalized MSE during hyperparameter tuning of the saturation model. Iteration 77 corresponds to the optimized parameter set.

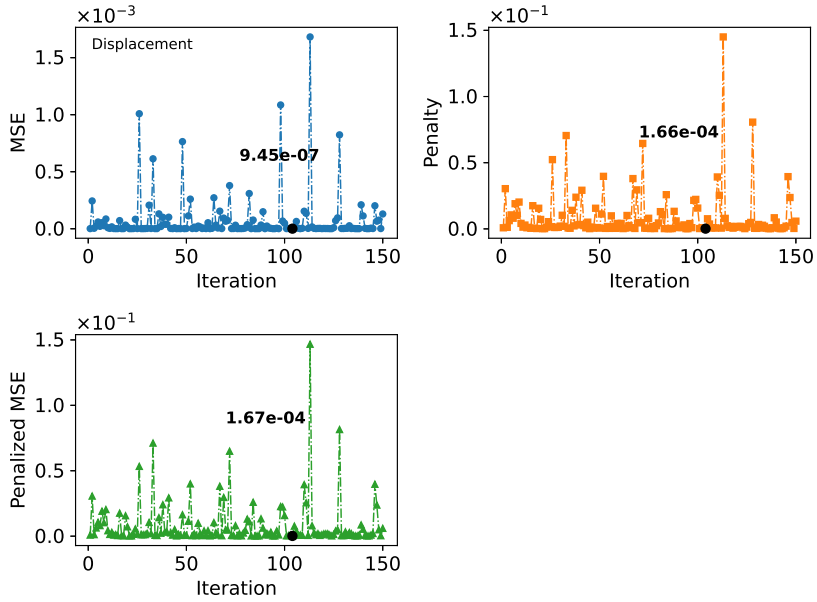

Figure 5: The evolution of MSE, penalty term, and penalized MSE during hyperparameter tuning of the displacement model. Iteration 104 corresponds to the optimized parameter set.

Table 3 shows consistency in hyperparameters such as maximum depth (16) and learning rate (0.25), indicating that deeper trees and relatively higher learning rates are needed to capture the complex relationships in the data. The regularization parameters λ and α are fixed at 1.0 for the saturation and displacement models, indicating that minimal regularization is sufficient to achieve optimal performance in these models. In contrast, the porosity model requires a higher λ value (6.0), suggesting stronger regularization to avoid overfitting. In addition, the number of estimators is nearly maximized for the saturation and displacement models (594 and 593), while the porosity model stabilizes at a slightly lower value (497).

Table 3: Hyperparameter ranges and optimized values for CatBoost models.

Hyperparameter	Range	Models		
		Porosity	Saturation	Displacement
n_estimators	100 to 600	497	594	593
max_depth	3 to 16	16	16	16
η	0.01 to 0.25	0.25	0.25	0.25
λ	1 to 6	6.0	1.0	1.0
α	1 to 5	1.0	1.0	1.0

The model performance metrics in Table 4 show high prediction accuracy and generalization for all three models. The porosity model achieved near-perfect R^2 values of 0.9999 and a root mean square error (RMSE) of 0.0001 for both training and test datasets. Similarly, the saturation model achieved R^2 values of 0.9991 with RMSE values of 0.007 (training) and 0.0072 (test), indicating reliable performance even with potentially more variable data. The displacement model also achieved R^2 values of 0.9999 and an RMSE of 0.001 m on both data sets, confirming its accuracy and compliance with residual constraints.

The residuals of the porosity model for both training and test data sets exhibit a narrow range, with means close to zero and standard deviations of 0.0001, demonstrating the model's ability to make accurate predictions with negligible bias. The saturation model shows a slightly wider residual variability, with training residuals ranging from -0.665 to 0.708 and test residuals ranging from -0.91 to 0.969. Despite the wider range, mean residuals of zero and standard deviations of 0.007 indicate strong performance in capturing the complex relationships associated with saturation in both data sets.

The displacement model has narrow residual ranges, confirming the model's effectiveness in handling

Table 4: Model performance metrics.

Model	Train		Test	
	R^2	RMSE	R^2	RMSE
Porosity (-)	0.9999	0.0001	0.9999	0.0001
Saturation (-)	0.9991	0.007	0.9991	0.0072
displacement (m)	0.9999	0.001	0.9999	0.001

quadratic penalties. The residuals are distributed around zero with standard deviations of 0.001. Overall, the residual distributions validate the metrics in Table 4, confirming the robustness of the framework. The consistency of near-zero residual means across models and datasets suggests minimal systematic bias, while the tight distributions demonstrate the ability of the models to generalize effectively.

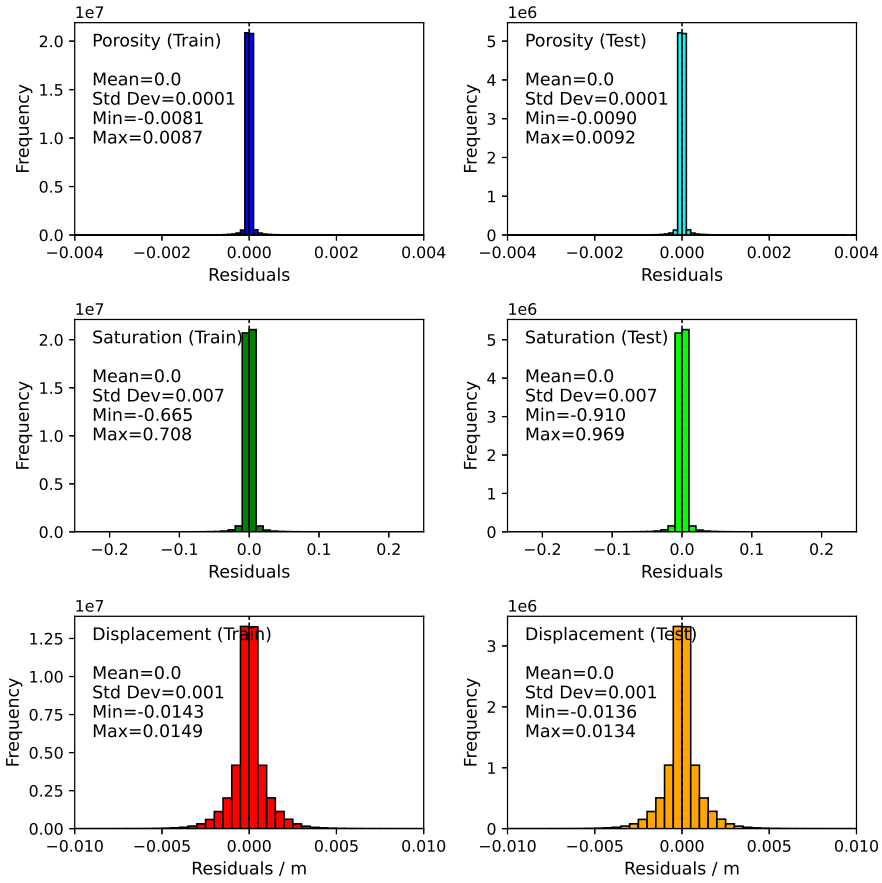

Figure 6: Residual distributions for the train and test datasets of the saturation, porosity, and displacement models.

Figure 7 shows the development of ground heave at post leakage (790 days) and post mitigation period (1490 days). The finite element and ML models replicate the shape and extent of ground surface heave, aligning with field observations from the geodetic monitoring network established by LGRB (2010, 2012). The models are sufficiently accurate from a practical perspective. Discrepancies between the modeled and observed field data can be attributed to simplifying assumptions inherent in the finite element model. For example, previous studies have shown that the gypsification of anhydrite, the primary process governing the swelling of clay-sulfate rocks, cannot be fully captured by hydro-mechanical models (Taherdangkoo et al., 2023; Wittke, 2014). In such models, swelling is driven by changes in the pore water saturation and once the pore space becomes saturated, the swelling process is considered completed. In reality, however, the complete transformation of anhydrite into gypsum rarely occurs.

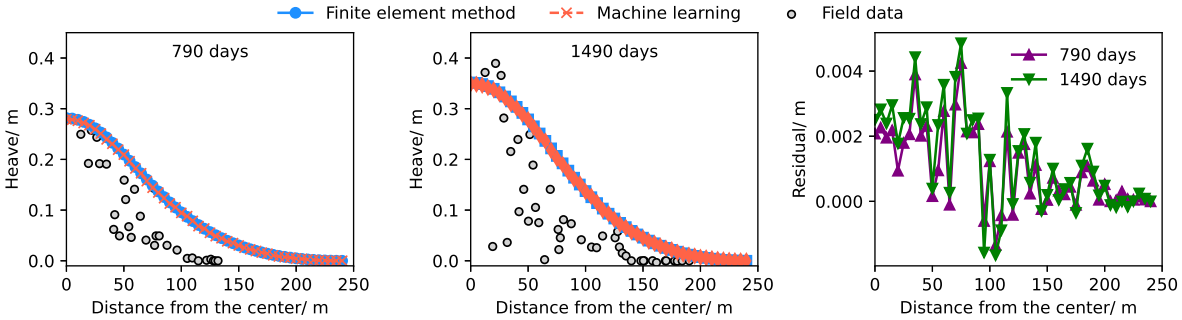

Figure 7: Comparison of geodetic heave measurements with simulated heave using the finite element and machine learning models for two points in time: post-leakage (790 days) and post-mitigation (1490 days). The modeling residuals are shown.

The ML model shows predictive accuracy comparable to the finite element method while offering significant computational efficiency. The residuals, shown in the right panel of Figure 7, are primarily within $\pm 0.003\,\mathrm{m}$ and show no discernible spatial bias. The residuals have near-zero means ($0.001\,\mathrm{m}$ at 790 days and $0.0013\,\mathrm{m}$ at 1490 days) as well as small standard deviations ($0.0012\,\mathrm{m}$ and $0.0015\,\mathrm{m}$).

Figure 8 and Figure 9 show the spatial distributions of porosity, saturation, and displacement across the model domain at 790 and 1490 days. Porosity predictions show minimal changes, consistent with the slow evolution of volumetric strain in clay-sulfate rocks and the uniform material properties of the swelling layer. Saturation distributions show the evolution of the water front due to water ingress, the primary trigger of swelling processes. Displacement predictions accurately represent the swelling-induced ground heave, showing steep gradients in the vicinity of the swelling center that attenuate with distance due to the absence of swelling pressures in the far field. The comparison between the two time steps demonstrates the effectiveness of mitigation strategies as evidenced by the reduced water intrusion and associated swelling.

The porosity residuals show minimal spatial variation across the domain with the exception of the saturation front. The saturation residuals show greater variability in regions where water flow dynamics are more complex, such as near saturation fronts. The displacement residuals are slightly larger near regions with steep displacement gradients. The analysis shows the limitations of the model in fully reproducing the FEM predictions under nonlinear conditions. However, the residuals remain small, indicating that the model has high fidelity in replicating the nonlinear flow and mechanical responses.

6.2 Sensitivity analysis

Consistent with previous HM studies (Schädlich et al., 2013; Taherdangkoo et al., 2022a), sensitivity analysis (Figure 10) revealed that the model is most sensitive to changes in maximum swelling pressure and Young's modulus. The strong linear relationship between swelling pressure and displacement indicates the importance of accurately characterizing these parameters for predictive modeling. Poisson's ratio, permeability, and air entry pressure also influenced the model, although to a lesser extent. These results are consistent with previous parametric studies conducted for swelling-prone clay formations.

The variation trends in the FEM and ML models for all parameters are in close agreement, with the ML model successfully capturing the shape, magnitude, and extent of the heave at the ground surface over the entire sensitivity range. Furthermore, the performance of the ML model demonstrates its ability to generalize over a wide range of parameter values without introducing significant biases or deviations, reinforcing its suitability for practical applications in site-specific analysis. The close fit also confirms the potential of the hybrid framework to accurately simulate complex nonlinear processes with reduced computational requirements.

6.3 Uncertainty quantification

The uncertainty associated with the porosity, saturation, and displacement predictions was evaluated using Monte Carlo simulations with a sample size of $N = 30\,000$. The statistical metrics and corresponding

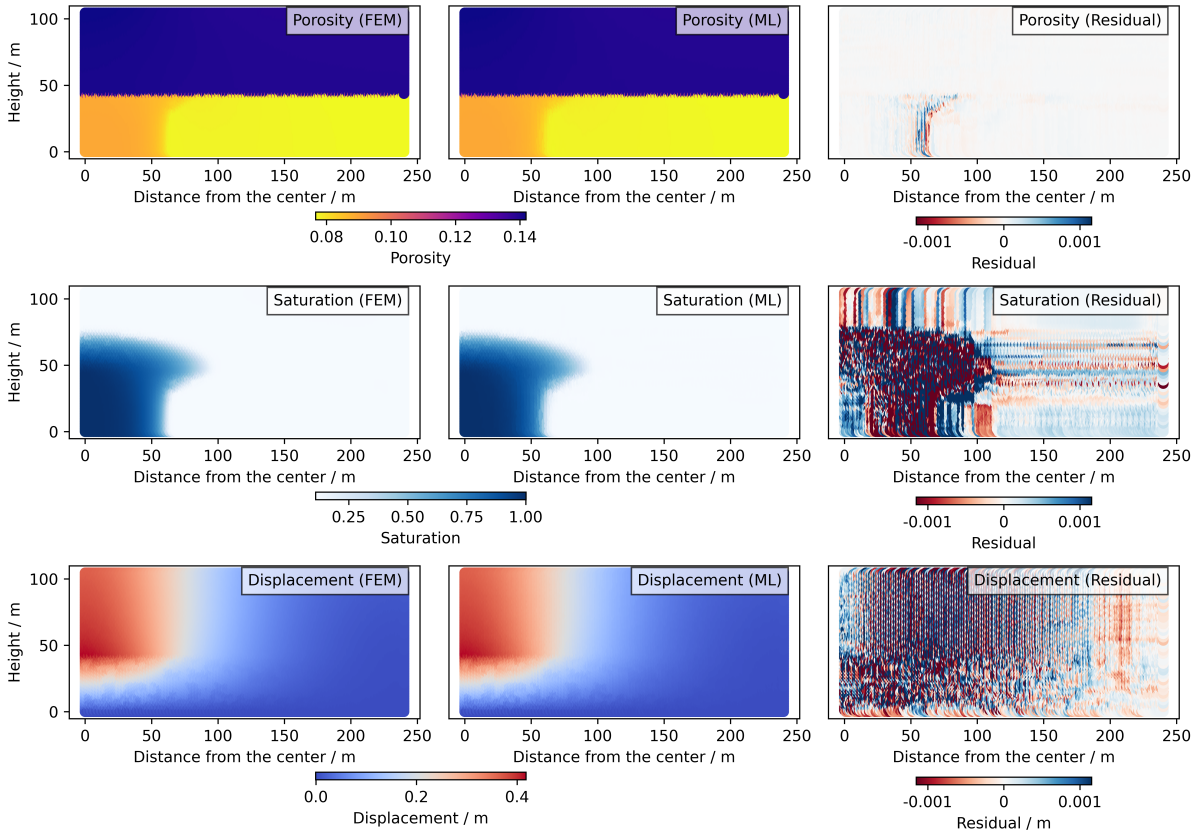

Figure 8: Comparison of porosity, saturation, and displacement predicted by the finite element and the machine learning models across the spatial domain at 790 day. The modeling residuals are depicted in the right panel.

confidence intervals derived from the analysis are summarized in Table 5 and Figure 11.

Table 5: Comparison of uncertainty quantification metrics for marginalized predictions.

	Mean	Std. Dev.	COV	q_1	q_{25}	q_{50} (Median)	q_{75}	q_{99}
Porosity (-)	0.115	0.009	0.082	0.086	0.110	0.116	0.121	0.137
Saturation (-)	0.223	0.216	0.968	0.028	0.120	0.129	0.212	0.991
Displacement (m)	0.063	0.025	0.399	0.015	0.053	0.064	0.069	0.164

Porosity has a mean of 0.115 with a standard deviation of 0.009 and a variance of approximately 0.00008. This relatively small variability is further reflected in the moderately narrow interquartile (IQR) range, where $q_{25} = 0.110$ and $q_{75} = 0.121$ are closely spaced around the median $q_{50} = 0.116$. These results suggest that saturation predictions are stable, potentially due to the less dynamic nature of this rock property in the swelling layer, where spatial variations are relatively minimal. The upper outliers appear mostly beyond $q_{99} = 0.137$.

Saturation, by contrast, exhibits the highest variability among the three parameters, with a mean of 0.223, a standard deviation of 0.216, and a variance of 0.04666. This extensive spread is further evidenced by the wide IQR, where $q_{25} = 0.120$ and $q_{75} = 0.212$ are far away from the median $q_{50} = 0.129$. These results indicate a high sensitivity of the saturation predictions to uncertainties in the input parameters, reflecting its dynamic behavior.

Displacement has a mean of 0.063, a standard deviation of 0.025, and a variance of 0.00063. Although it displays greater variability than porosity, it remains more constrained than saturation. The quantiles $q_1 = 0.015$ and $q_{99} = 0.164$ indicate the influence of localized swelling effects and nonlinear deformations, but the interquartile values $q_{25} = 0.053$ and $q_{75} = 0.069$ are relatively close to the median $q_{50} = 0.064$.

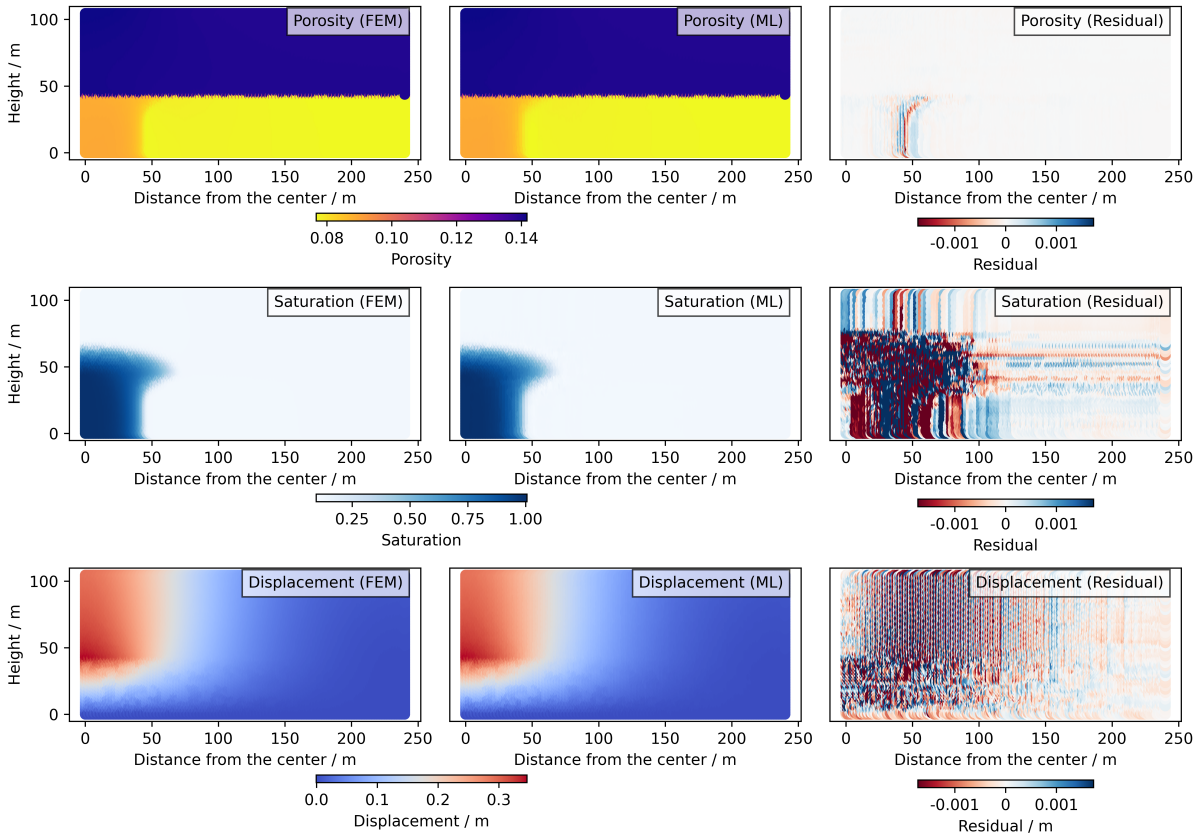

Figure 9: Comparison of porosity, saturation, and displacement predicted by the finite element and the machine learning models across the spatial domain at 1490 day. The modeling residuals are depicted in the right panel.

7 Conclusion

This study presents a hybrid framework based on a hydro-mechanical model previously developed to analyze the swelling of clay-sulfate rocks at the Staufen study site (Taherdangkoo et al., 2022a). The framework predicts water front propagation and its effect on porosity and displacement with high accuracy, providing a balance between computational efficiency and prediction accuracy. The small residuals and lack of systematic bias demonstrate the model's reliability for the regression task. Sensitivity analysis shows the importance of site-specific parameters such as swelling pressure, permeability, and Young's modulus, emphasizing the importance of accurate site-specific characterization of material properties. Uncertainty quantification through Monte Carlo simulations confirms the robustness of the model and validates its suitability for long-term, nonlinear swelling processes.

A key advantage of this hybrid approach is the balance between computational efficiency and predictive accuracy. By using a machine learning surrogate, the framework enables fast simulations suitable for real-time applications and extensive parametric studies. The inclusion of penalties ensures that the predictions remain meaningful, making the framework adaptable to different geotechnical scenarios. The framework thus provides a valuable alternative for risk assessment, engineering design, and mitigation planning in regions affected by swelling. Overall, the work demonstrates the utility of machine learning as a computationally efficient approximation method in geotechnical applications.

However, the reliance on synthetic data sets generated by FEM simulations may not fully capture real-world complexities, such as field-specific conditions. Extending the framework with physics-informed neural networks (PINNs) (Raissi et al., 2019) to improve enforcement of physical constraints and continual learning could further enhance its capability for large-scale studies. Future efforts could extend the framework to broader applications, such as tunneling, slope stability, and foundation design in geologically active areas.

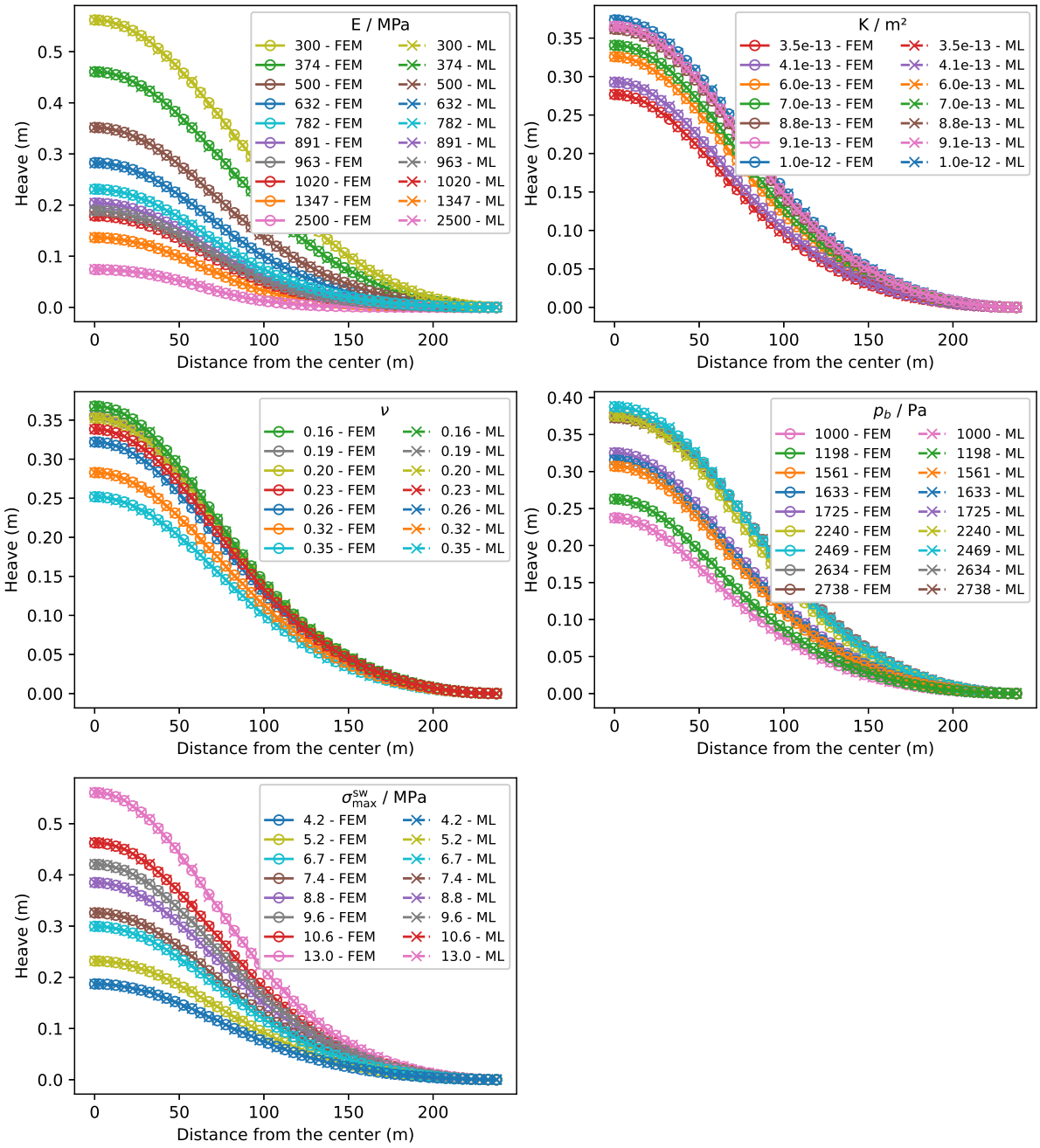

Figure 10: Sensitivity analysis of various parameters on heave calculated from finite element and machine learning approaches. The heave at the ground surface at 1490 day is plotted, varying Young's modulus, permeability, Poisson's ratio, air entry pressure, and maximum swelling pressure of the swelling layer.

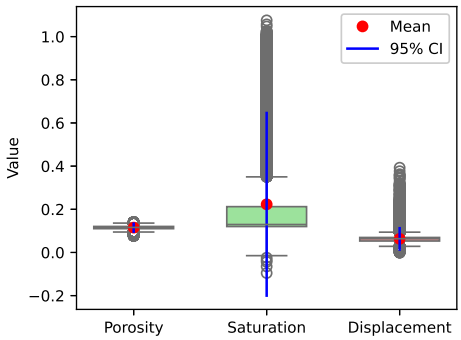

Figure 11: Box plot of porosity, saturation and displacement with whiskers representing data spread, mean values marked in red, 95% confidence intervals as blue lines, and outliers as individual points beyond the whiskers, indicating extreme variations in the data.

Funding

This research is funded by the German Research Foundation (DFG) for project TA 2076/1-1.

Competing Interests

The authors declare no competing interests.

Code Availability

The machine learning code used in this study was developed using Jupyter Notebook and is available upon request from the corresponding author.

CRediT authorship contribution statement

Reza Taherdangkoo: Conceptualization, Methodology, Validation, Formal analysis, Funding acquisition, Writing - Original Draft. **Mostafa Mollaali**: Methodology, Formal analysis, Writing - Review & Editing. **Matthias Ehrhardt**: Methodology, Writing - Review & Editing. **Thomas Nagel**: Writing - Review & Editing. **Lyesse Laloui**: Writing - Review & Editing. **Alessio Ferrari**: Writing - Review & Editing. **Christoph Butscher**: Writing - Review & Editing. All authors contributed to discussions of the results and their implications.

References

Alonso, E. (2023). The positive history of an error. modelling the heave of a nuclear power station. *E3S Web of Conferences*, *382*, 00002.

Benz, T., & Wehnert, M. (2012). *Schadensfall Staufen im Breisgau – Zweiter Bericht zu den Berechnungen der zeitlichen Entwicklung der Hebungsprozesse*.

Bilke, L., Flemisch, B., Kalbacher, T., Kolditz, O., Helmig, R., & Nagel, T. (2019). Development of Open-Source Porous Media Simulators: Principles and Experiences. *Transport in Porous Media*, *130*(1), 337–361.

Buchwald, J., Kolditz, O., & Nagel, T. (2024). Design-of-experiment (doe) based history matching for probabilistic integrity analysis—a case study of the fe-experiment at mont terri. *Reliability Engineering & System Safety*, *244*, 109903.

Buchwald, J., Chaudhry, A., Yoshioka, K., Kolditz, O., Attinger, S., & Nagel, T. (2020). Doe-based history matching for probabilistic uncertainty quantification of thermo-hydro-mechanical processes around heat sources in clay rocks. *International Journal of Rock Mechanics and Mining Sciences*, *134*, 104481.

Burden, F., & Winkler, D. (2009). Bayesian regularization of neural networks. In *Artificial neural networks: Methods and applications* (pp. 23–42). Humana Press.

Butscher, C., Mutschler, T., & Blum, P. (2016). Swelling of clay-sulfate rocks: A review of processes and controls. *Rock Mechanics and Rock Engineering*, *49*(4), 1533–1549.

Butscher, C., Huggenberger, P., Zechner, E., & Einstein, H. H. (2011). Relation between hydrogeological setting and swelling potential of clay-sulfate rocks in tunneling. *Engineering Geology*, *122*(3-4), 204–214.

Chaudhry, A. A., Nagel, T., Zhao, J., Düsterloh, U., Zhao, J., Chen, L., Wang, J., Liu, Y., Cao, S., Zhang, Q., Shao, H., Chen, C., Yuan, T., Lu, R., Fischer, C., & Kolditz, O. (2024). Model analysis. In H. Shao, J. Wang, T. Schäfer, C.-L. Zhang, H. Geckeis, T. Nagel, U. Düsterloh, O. Kolditz, & H. Shao (Eds.), *Thermo-hydro-mechanical-chemical (THMC) processes in bentonite barrier systems* (pp. 91–138). Springer Nature Switzerland.

Dorogush, A. V., Ershov, V., & Gulin, A. (2018). Catboost: Gradient boosting with categorical features support. *arXiv preprint arXiv:1810.11363*.

Foresee, F. D., & Hagan, M. T. (1997). Gauss-Newton approximation to Bayesian learning. *Proceedings of international conference on neural networks (ICNN'97)*, *3*, 1930–1935.

Grimm, M., Stober, I., Kohl, T., & Blum, P. (2014). Schadensfallanalyse von Erdwärmesondenbohrungen in Baden-Württemberg. *Grundwasser*, *19*(4), 275–286.

Jarzyna, A., Bąbel, M., Ługowski, D., & Vladi, F. (2022). Petrographic record and conditions of expansive hydration of anhydrite in the recent weathering zone at the abandoned dingwall gypsum quarry, Nova Scotia, Canada.

Kafle, L., Xu, W.-j., Zeng, S.-y., & Nagel, T. (2022). A numerical investigation of slope stability influenced by the combined effects of reservoir water level fluctuations and precipitation: A case study of the Bianjiazhai landslide in China. *Engineering Geology*, *297*(May 2021), 106508.

Kolditz, O., Bauer, S., Bilke, L., Böttcher, N., Delfs, J. O., Fischer, T., Görke, U. J., Kalbacher, T., Kosakowski, G., McDermott, C. I., Park, C. H., Radu, F., Rink, K., Shao, H., Shao, H. B., Sun, F., Sun, Y. Y., Singh, A. K., Taron, J., … Zehner, B. (2012). OpenGeoSys: an open-source initiative for numerical simulation of thermo-hydro-mechanical/chemical (THM/C) processes in porous media. *Environmental Earth Sciences*, *67*(2), 589–599.

Kooti, G., Dabir, B., Butscher, C., & Taherdangkoo, R. (2024). A constrained machine learning surrogate model to predict the distribution of water-in-oil emulsions in electrostatic fields. *Scientific Reports*, *14*(1), 11142.

LGRB. (2010). *Geologische Untersuchungen von Baugrundhebungen im Bereich des Erdwärmesondenfeldes beim Rathaus in der historischen Altstadt von Staufen i. Br. (Tech. Rep.): Landesamt für Geologie, Rohstoffe und Bergbau (LGRB)*. https://lgrbwissen.lgrb-bw.de/sites/default/files/public/lgrbwissen/dokumente/lgrb-dokumente-sachstandsbericht-2010-ews-schadensfall-staufen-mit-anlagenx.pdf

LGRB. (2012). *Zweiter Sachstandsbericht zu den seit dem 01.03.2010 erfolgten Untersuchungen im Bereich des Erdwärmesondenfeldes beim Rathaus in der historischen Altstadt von Staufen i. Br. Landesamt für Geologie, Rohstoffe und Bergbau (LGRB)*. https://lgrbwissen.lgrb-bw.de/sites/default/files/public/lgrbwissen/dokumente/lgrb-dokumente-sachstandsbericht-2012-ews-schadensfall-staufen-mit-anlagen.pdf

Madsen, F. T., & Müller-Vonmoos, M. (1989). The swelling behaviour of clays. *Applied Clay Science*, *4*(2), 143–156.

Metropolis, N., & Ulam, S. (1949). The Monte Carlo method. *Journal of the American Statistical Association*, *44*(247), 335–341.

Pitz, M., Kaiser, S., Grunwald, N., Kumar, V., Buchwald, J., Wang, W., Naumov, D., Chaudhry, A. A., Maßmann, J., Thiedau, J., Kolditz, O., & Nagel, T. (2023). Non-isothermal consolidation: A systematic evaluation of two implementations based on multiphase and richards equations. *International Journal of Rock Mechanics and Mining Sciences*, *170*, 105534.

Prokhorenkova, L., Gusev, G., Vorobev, A., Dorogush, A. V., & Gulin, A. (2018). Catboost: Unbiased boosting with categorical features. *Advances in Neural Information Processing Systems*, *31*.

Raissi, M., Perdikaris, P., & Karniadakis, G. E. (2019). Physics-informed neural networks: A deep learning framework for solving forward and inverse problems involving nonlinear partial differential equations. *J. Comput. Phys.*, *378*, 686–707.

Ruch, C., & Wirsing, G. (2013). Erkundung und Sanierungsstrategien im Erdwärmesonden-Schadensfall Staufen i. Br. (exploration and rehabilitation strategies in case of damaging geothermal heat exchangers in Staufen i. Br.) *Geotechnik*, *36*(3), 147–159.

Schädlich, B., Marcher, T., & Schweiger, H. (2013). Application of a constitutive model for swelling rock to tunnelling. *Geotech Engineering*, *44*(3), 47–54.

Schweizer, D., Prommer, H., Blum, P., Siade, A. J., & Butscher, C. (2018). Reactive transport modeling of swelling processes in clay-sulfate rocks. *Water Resources Research*, *54*(9), 6543–6565.

Schweizer, D., Prommer, H., Blum, P., & Butscher, C. (2019). Analyzing the heave of an entire city: Modeling of swelling processes in clay-sulfate rocks. *Engineering Geology*, *261*, 105259.

Snoek, J., Larochelle, H., & Adams, R. P. (2012). Practical Bayesian optimization of machine learning algorithms. *Advances in neural information processing systems*, *25*.

Taherdangkoo, R., Abdallah, N. M., & Butscher, C. (2024a). Comparative evaluation of hydro-mechanical models in swelling of clay-sulfate rocks: Case study of Staufen, Germany. *Computers and Geotechnics*, *170*, 106286.

Taherdangkoo, R., Yang, H., Akbariforouz, M., Sun, Y., Liu, Q., & Butscher, C. (2021). Gaussian process regression to determine water content of methane: Application to methane transport modeling. *Journal of Contaminant Hydrology*, *243*, 103910.

Taherdangkoo, R., Nagel, T., Tang, A. M., Pereira, J.-M., & Butscher, C. (2022a). Coupled hydro-mechanical modeling of swelling processes in clay-sulfate rocks. *Rock Mechanics and Rock Engineering*, *55*(12), 7489–7501.

Taherdangkoo, R., Meng, T., Amar, M. N., Sun, Y., Sadighi, A., & Butscher, C. (2022b). Modeling solubility of anhydrite and gypsum in aqueous solutions: Implications for swelling of clay-sulfate rocks. *Rock Mechanics and Rock Engineering*, *55*(7), 4391–4402.

Taherdangkoo, R., Barsch, M., Ataallah, A., Meng, T., Liu, Q., & Butscher, C. (2023). A hydro-mechanical approach to model swelling tests of clay-sulfate rocks. *Rock Mechanics and Rock Engineering*, 1–12.

Taherdangkoo, R., Nagel, T., Chen, C., Mollaali, M., Ghasabeh, M., Cuisinier, O., Abdallah, A., & Butscher, C. (2024b). Modeling unsaturated hydraulic conductivity of compacted bentonite using a constrained catboost with bootstrap analysis. *Applied Clay Science*, 107530.

Van Genuchten, M. T. (1980). A closed-form equation for predicting the hydraulic conductivity of unsaturated soils. *Soil Science Society of America Journal*, *44*(5), 892–898.

Virupaksha, A. G., Nagel, T., Lehmann, F., Rajabi, M. M., Hoteit, H., Fahs, M., & Ber, F. L. (2024). Modeling transient natural convection in heterogeneous porous media with convolutional neural networks. *International Journal of Heat and Mass Transfer*, *222*, 125149.

Wanninger. (2020). Experimental investigations for the modelling of anhydritic swelling claystones. vdf Hochschulverlag AG.

Wittke, W. (2014). Swelling rock. In *Rock mechanics based on an anisotropic jointed rock model (AJRM)* (pp. 181–208). John Wiley & Sons, Ltd.